

1           **Limitations in one-dimensional (an)elastic Earth**  
2           **models for explaining GPS-observed M<sub>2</sub> Ocean Tide**  
3           **Loading displacements in New Zealand**

4           **Bogdan Matviichuk<sup>1</sup>, Matt A. King<sup>1</sup>, Christopher S. Watson<sup>1</sup> and Machiel S.**  
5           **Bos<sup>2\*</sup>**

6           <sup>1</sup>School of Geography, Planning, and Spatial Sciences, University of Tasmania, Hobart, 7001, Australia  
7           <sup>2</sup>Instituto Dom Luiz (IDL), University of Beira Interior, Covilhã, Portugal

8           **Key Points:**

- 9           • M<sub>2</sub> ocean tide loading displacements in New Zealand are inferred from GPS ob-  
10           servations  
11           • Estimates for the North Island are not reproduced by models combining ocean tide  
12           loading and a 1D (an)elastic Earth structure  
13           • Spatially-coherent residual displacements of  $\sim 0.4$  mm (2%) are likely due to lat-  
14           eral Earth structure associated with Pacific Plate subduction

---

\*supported by the project FCT/UIDB/50019/2020 – IDL funded by FCT

Corresponding author: B. Matviichuk, [bogdan.matviichuk@utas.edu.au](mailto:bogdan.matviichuk@utas.edu.au)

**Abstract**

[GPS observations of ocean tide loading displacements can help infer the regional anelastic properties of the asthenosphere. We estimate  $M_2$  ocean tide loading displacements at 170 GPS sites in New Zealand and compare these to modeled values using a range of numerical tide and radially symmetric (1D) elastic and anelastic Earth models. Regardless of the model combination we are unable to reduce the strong spatial coherence of the  $M_2$  residuals across the North Island where they reach 0.4 mm (2%). The best fit in the North Island is obtained when combining the FES2014b tide model with spatially-variable ocean density and water compressibility, and the STW105 Earth model. The residuals exhibit a change of  $\sim 0.3$  mm in magnitude between the Taupo Volcanic Zone and the east coast ( $\sim 100$  km), suggesting that this region's laterally-varying, shallow rheological structure may need to be considered to explain these observations.]

**Plain Language Summary**

[The solid Earth changes shape due to the changing weight of the ocean as the ocean tides rise and fall. Measuring this change and comparing it to predictions can yield insights into the interior properties of the Earth, tens to hundreds of kilometers below the surface. We used GPS to measure the changing shape of New Zealand and compared it to predictions based on a range of Earth and tide models. The difference between the observed and modeled displacements revealed a complicated pattern over New Zealand, especially in the North Island and specifically near the Taupo Volcanic Zone. Due to the high accuracy of our GPS analysis and the ocean tide models, the observed residuals provide information about the elastic properties of the Earth and the complex geological structure of the region. The observed significant misfits show limitations of the 1D Earth model that varies only with depth which is standard in geodetic analysis.]

**1 Introduction**

The asthenosphere, the weak viscoelastic substrate beneath the lithosphere, is fundamental to the concept of plate tectonics and the earthquake cycle (Hu et al., 2016). The rheological properties of the asthenosphere are, however, not well understood (Karato, 2012). The importance of the asthenosphere is amplified at active convergent boundaries of tectonic plates, specifically subduction systems that initiate forces principal in driving plate tectonics and mantle convection (Stern, 2004). New Zealand is split by the transform Alpine Fault and is locked between two subduction systems: the Hikurangi in the north and Puysegur in the south (Lamarche & Lebrun, 2000). These lithospheric discontinuities should produce the large perturbations observable in the earth tide and perhaps the ocean load tide displacements (Zürn et al., 1976).

Analysis of Ocean Tide Loading, a phenomenon created by the solid Earth's response to tidal-water mass redistribution, can be used to validate ocean tide models and elastic Earth models at tidal periods (e.g., Farrell, 1972b; Martens et al., 2016; Yuan et al., 2013; Yuan & Chao, 2012). More recently GPS-derived Ocean Tide Loading Displacements (OTLD) have been used to constrain the asthenosphere's anelasticity at the period of the major  $M_2$  tidal constituent (period of 12.42 h) by showing improved agreement with deformation modeled using anelastic Earth models. To date, studies of asthenosphere anelasticity have focused on continental settings such as western Europe, western USA, South America, the eastern China Sea region and Alaska (Bos et al., 2015; Ito & Simons, 2011; Martens & Simons, 2020; Wang et al., 2020).

In this paper, we examine the tidal deformation of New Zealand, at the dominant  $M_2$  tidal period, using an array of continuous GPS stations. We combine recent ocean tide models with a range of purely elastic and anelastic 1D Earth models and compare modeled deformation with GPS observed estimates to further understand the anelastic properties of the asthenosphere beneath New Zealand.

## 2 Methods

### 2.1 GPS Data and Analysis

We analyzed all available continuously operating GNSS stations in New Zealand over the period from the beginning of 2013 to mid-2020 (doy 153), chosen to maximize the number of stations with overlapping data and minimize data gaps in individual stations. Over this seven-year period, data are available from 170 stations, with all but two (CHTI and RAUL) located on mainland New Zealand (see Table S1 for a full list of sites). These stations were designed for nationwide coverage with station spacing in the range 80–100 km to monitor and control the national datum and for geophysical studies (Gale et al., 2015). As shown in Fig. 1, the network provides approximately uniform (but sparse) coverage in the South Island with a substantially higher spatial density of coverage across much of the North Island.

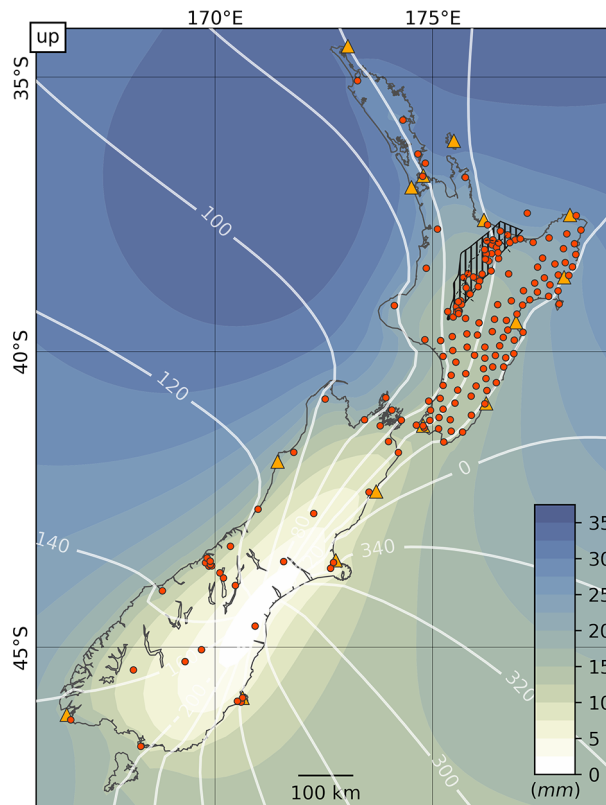


**Figure 1.** Map of New Zealand showing modeled  $M_2$  Up OTLD amplitude and phase (relative to Greenwich) computed with TPXO7.2 ocean tide model and PREM Green’s function. GPS sites and tide gauge locations are represented by red circles and orange triangles, respectively. The hatched area in the North Island represents the approximate region of the Taupo Volcanic Zone.

These data were analyzed using GipsyX v1.3 software (Bertiger et al., 2020) using a kinematic Precise Point Positioning (PPP) approach (Zumberge et al., 1997). The dataset processing was facilitated by a custom wrapper (Matviichuk, 2020). Our approach was described in full by Matviichuk et al. (2020) with the main difference being that here we used only the GPS data. Data from other GNSS (e.g. GLONASS) were not logged at all sites over this period hence was excluded from this analysis. We used NASA JPL’s orbit and clock products from their third internal reprocessing campaign (repro

3.0, released March 2018). Ambiguities were fixed to integers where possible (Bertiger et al., 2010). Earth body tides were modeled within GipsyX according to IERS 2010 Conventions (Petit & Luzum, 2010). A priori OTLD values were removed based on the FES2004 ocean tide model (Lyard et al., 2006) and Gutenberg-Bullen purely-elastic Earth model (Farrell, 1972a) in a centre-of-mass of the whole Earth system frame (`holt.oso.chalmers.se/loading`) – we later restored the OTLD component at the coordinate time series level for further study; this remove-restore approach is done to reduce the magnitude of companion tides and follows approaches adopted previously (e.g., Abbaszadeh et al., 2020; Matviichuk et al., 2020; Penna et al., 2015).

The GipsyX coordinate and zenith-wet-delay process noise values were chosen based on the tests of Penna et al. (2015), Wang et al. (2020) and Matviichuk et al. (2020), using values of 3.2 mm/sqrt(s) and 0.1 mm/sqrt(s), respectively. Our parameterization produces coordinate estimates every 300 s from which we remove large outliers identified with clock bias estimates larger than  $3 \times 10^3$  meters and residuals to a detrended timeseries that are larger than  $\pm 3\sigma$  of each global cartesian coordinate component. These timeseries were converted to local topocentric east, north and up components which were then further analyzed.

## 2.2 OTLD Models

We focus here on the difference between the GPS-derived OTLD and those modeled based on ocean tide models and elastic and anelastic Earth models. For the tides we mainly consider three relatively recent global ocean tide models: GOT4.10c (Ray, 2013), TPXO9.v1 (Egbert & Erofeeva, 2002) and FES2014b (Carrere et al., 2016), although we also explore FES2012 (Carrere et al., 2013) and FES2004 (Lyard et al., 2006). We also consider one regional New Zealand tide model (Walters et al., 2001), EEZ, which we combine with FES2014b outside the model’s domain for loading computations. We used bicubic interpolation to resample the models to a common  $0.05 \times 0.05^\circ$  grid. We note that the TPXO9.v2a model was also later analyzed but we found no improvement relative to TPXO9.v1 model present in the analysis.

The amplitude of the  $M_2$  tide reaches over 1 m near the coast of New Zealand, due to the shallow bathymetry, and decreases to 10-20 cm in the open ocean (Stammer et al., 2014). The pattern of  $M_2$  between the two islands of New Zealand is similar to an amphidromic point although the amplitudes are not zero. As a result, the tides to the east and west of New Zealand are out of phase and partly cancel out each other’s contribution to the total OTLD value in the up component.

All modeled OTLD values were computed using the CARGA software (Bos & Baker, 2005). The coastline was taken from the GMT database (Wessel & Smith, 1996) and has a resolution of around 150 m. In most studies a constant sea water density is assumed, for example  $1030 \text{ kg/m}^3$ . Ray (2013) advocated to take the spatial variation of the density into account, and even the fact that water is slightly compressible, which means that the mean density of a water column should increase due to the extra density at the bottom of the column. For the ocean around New Zealand the effect on the resultant deformation is around 1-3%. Assuming a mean 2% effect and a mean OTLD amplitude of 20 mm, this corresponds to a potential error of 0.4 mm which is too large to be ignored. We have implemented the equations of Ray (2013) and obtained mean density values from the World Ocean Atlas 2013 - WOA13 (Zweng et al., 2013) based on a  $0.25 \times 0.25^\circ$  grid.

Three Green’s functions were assessed with this set of ocean tide models: PREM (Dziewonski & Anderson, 1981), STW105 (Kustowski et al., 2008) and S362ANI (Kustowski et al., 2008). PREM and STW105 provide radial (1D) profiles for the density, and seismic velocities  $V_p$  and  $V_s$ . These profiles were used to compute load Love numbers which were converted into Green’s functions (Bos & Scherneck, 2013). The method is based on Alterman et al. (1959) but uses the more recent Chebyshev collocation method to solve the differential equations (Guo et al., 2001). These profiles are based on seismic data and are only valid at a period of 1 s. To convert them to the period of the  $M_2$  constituent,

137 a constant absorption band ( $Q=\text{constant}$ , see Table S5) is assumed between these two  
 138 periods (Bos et al., 2015). S362ANI is based on STW105 but has a shear velocity that  
 139 varies horizontally, not just by depth. Given our focus on 1D radially symmetric mod-  
 140 els, we averaged the values in a rectangular region between  $48^\circ\text{S}$  and  $33^\circ\text{S}$  and  $165^\circ\text{E}$   
 141 and  $180^\circ\text{E}$  to yield a model representative of the average values over the study region.  
 142 Once converted into a radially symmetric model, the Green’s function for S362ANI was  
 143 computed in similar manner as PREM and STW105.

### 144 2.3 OTLD Analysis

145 Amplitudes and phases of tidal constituents, and their uncertainties, were estimated  
 146 from the GPS coordinate timeseries using the Eterna software v.3.30 (Wenzel, 1996) for  
 147 17 tidal constituents, with local phases converted to Greenwich phases with lags posi-  
 148 tive to enable comparison with the models of OTLD. Our focus is solely on the largest  
 149 loading constituent in New Zealand,  $M_2$ , the major semi-diurnal lunar constituent. To  
 150 decrease the computation time and measurement noise, the timeseries were first down-  
 151 sampled to 30-min through window averaging.

152 Before computing the residuals, we assessed the impact from the differences in the  
 153 ocean tide models on the modeled OTLD values. For this we computed errors associ-  
 154 ated with differences between the three global ocean tide models: FES2014b, GOT4.10c  
 155 and TPXO9.v1 (Fig. S3). The errors are consistent over most sites with a mean error  
 156 value of  $\sim 0.1$  mm in all three components. We follow the naming conventions of Yuan  
 157 and Chao (2012) with observed and modeled OTLD referred to as  $Z_{obs}$  and  $Z_{OTL}$  re-  
 158 spectively with  $Z_{res}$  being their vector difference. We refer to the magnitude of the vec-  
 159 tor difference as  $\|Z_{res}\|$ .

## 160 3 Results

### 161 3.1 Preliminary analysis of the ocean tide models

162 We expected local EEZ ocean tide model to perform similarly to the most recent  
 163 global tide models at the  $M_2$  period. We computed an average of the three most recent  
 164 ocean tide models: FES2014b, GOT4.10c, and TPXO9.v1 (Fig. 2a) to provide a base-  
 165 line for the assessment of the EEZ model. We added the FES2004 global model to the  
 166 comparison to assess the performance of global model recommended within the IERS  
 167 2010 Conventions for geodetic analysis (Petit & Luzum, 2010). Compared with the newer  
 168 global models, FES2004 demonstrated higher discrepancies (up to 1 m) in the semi-closed  
 169 water bodies and shallow bights (Fig. S1a), while the EEZ regional tide model shows  
 170 an approximately constant vector difference in the shallow sea waters ( $<1000$  m depth)  
 171 of around 0.1 m (Fig. S1b).

172 We assess the tide models further by comparing modeled  $M_2$  tide values with those  
 173 from 15 tide gauges, shown in Fig. 1. The mean of the  $M_2$  amplitude differences are shown  
 174 in Table 1 demonstrating that the EEZ model exhibits over 5-7 cm amplitude difference  
 175 relative to tide gauges. The other global models have mean amplitude differences of 1.13-  
 176 3.05 cm, with the GOT4.10c model in closest agreement in terms of mean amplitude dif-  
 177 ference at the tide gauges (see Table S5 for details).

178 To assess the variation between recent global ocean tide models at the  $M_2$  period  
 179 we computed the inter-model standard deviation (Fig. 2b). We found  $M_2$  standard de-  
 180 viation (SD) values of 0.18 cm and 2.68 cm for the deep ocean ( $>1000$  m depth) and the  
 181 shallow sea ( $<1000$  m depth) respectively. These values are smaller by 40% and 20% than  
 182 globally derived values reported by Stammer et al. (2014) for  $M_2$ . The largest SD val-  
 183 ues of up to 0.6 m are located in the Hauraki Gulf in the western North Island, which  
 184 indicates the region where the largest ocean tides errors are expected. We note however  
 185 that this is a very small region and hence will likely have negligible impact on most mod-  
 186 eled displacements considered here.

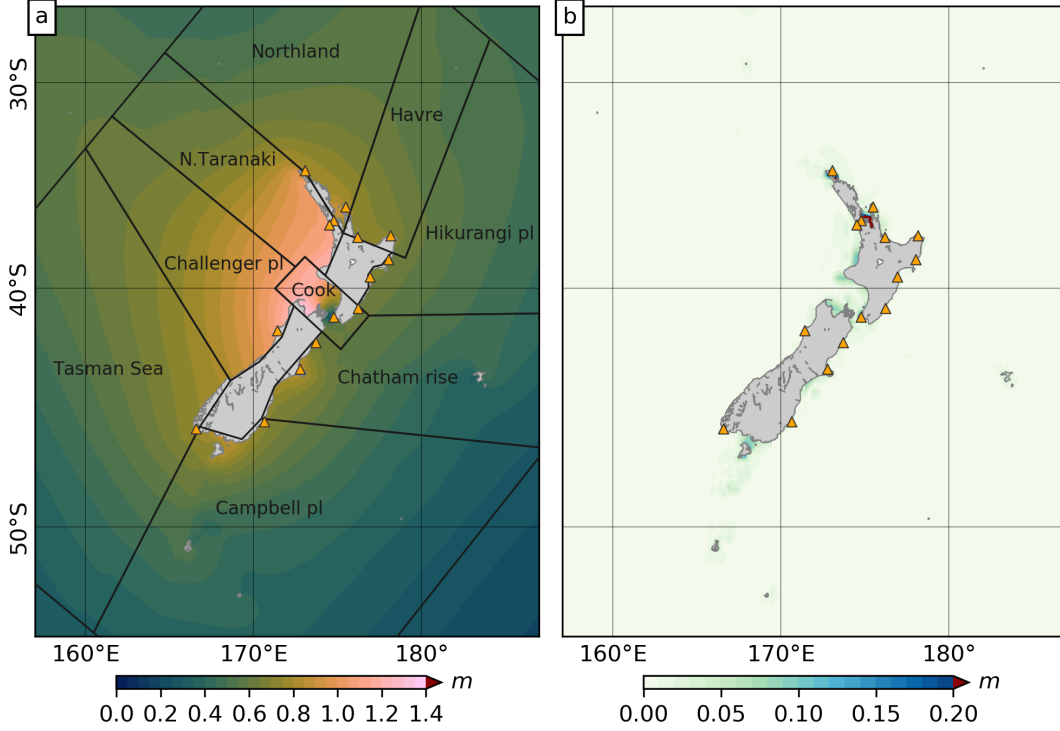


**Figure 2.** Comparison of recent global ocean tide models (FES2014b, GOT4.10c, TPXO9.v1) around New Zealand: (a)  $M_2$  tidal amplitudes computed as a mean of the ocean tide models. (b) Standard deviation (SD) of the vector differences between the global ocean tide models. The grey labeled polygons in (a) represent the areas used for OTLD phasor reconstruction. Note the scale extension above 0.2 m in (b) to demonstrate the high degree of agreement between these models with exception for  $\sim 1$  m SD on one small section of the north coast. Orange triangles represent tide gauges used in the analysis.

187

### 3.2 Comparison of GPS and PREM-based Models

188

189

190

191

192

193

194

195

196

197

198

199

200

201

202

203

204

205

The GPS-estimated  $M_2$  up OTLD (with the a priori model restored) are shown in Fig. 3 with horizontal components shown in Fig. S2, and listed in Table S2 for each of the up, north and east components. These show a spatially coherent signal across New Zealand with the amplitude ranging from 2 to 32 mm (sites WAIM and KTIA, respectively). Using these observations and the modeled  $Z_{OTL}$  based on FES2014b and PREM we computed  $Z_{res}$  as shown in Fig. 4a.  $M_2$  up residuals in the North Island are significant and demonstrate a spatially coherent amplitude of  $\sim 1$  mm and phase residual of  $\sim -10^\circ$ , while residuals in the South Island are small but harder to interpret due to the lower station density and the low OTLD amplitude (Fig. 1). This is consistent across different global ocean tide models as indicated by the  $\|Z_{res}\|$  values summarized in the boxplots (Fig. 4c, S4-5).  $\|Z_{res}\|$  variation over the range of tide models with PREM has median value of around 0.7 mm for any of the global tide models while the median for the EEZ model is  $\sim 2$  mm. This bias within the EEZ model results in a spatially coherent signal evident from the phasor maps (Fig. S6.2, up component), especially in the North Island.

While all the recent global ocean tide models perform similarly in the horizontal components, FES2014b demonstrates the largest reduction of  $\|Z_{res}\|$  over the set of Green's functions in the up component (Fig. S5).

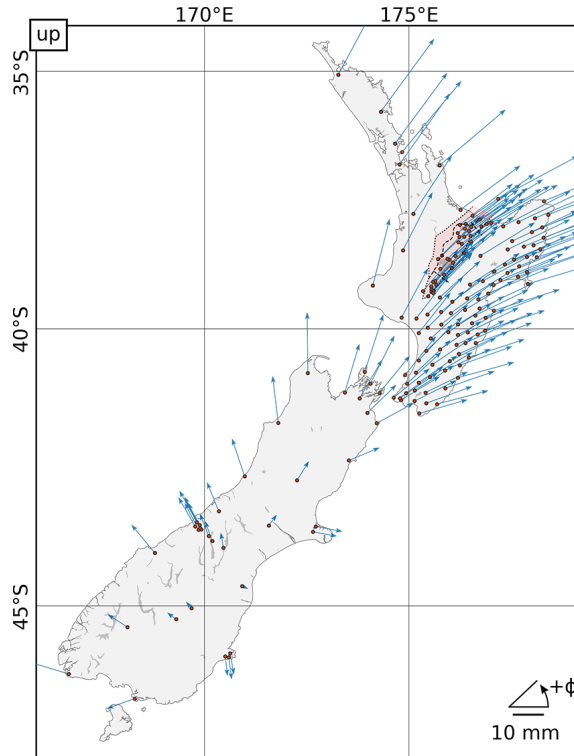


**Figure 3.** GPS-derived ocean tide loading displacements in the up component. Horizontal components are shown in Fig. S2

206 using FES2014b with orbits and clocks that were estimated with GOT4.8c may pro-  
 207 duce results associated with CoM modeling

208 Note that JPL used the GOT4.8ac tidal model (Desai & Ray, 2014) for OTLD mod-  
 209 eling which is inconsistent with the models tested here. This inconsistency may produce  
 210 results with residuals associated with CoM modeling. Thus we compared modeled re-  
 211 sults using FES2014b and GOT4.8c and found CoM differences values to be negligible  
 212 ( $\leq 0.01$  mm). We continue with FES2014b (Fig. 4c) as a baseline ocean tide model for  
 213 the subsequent tests.

214 We considered the impact on the total OTLD of specific water bodies by dividing  
 215 the global oceans into nine separate water areas surrounding New Zealand (Fig. 2). To  
 216 illustrate the influence of different regions, we selected three sites that experience high,  
 217 moderate and low  $M_2$  OTLD: KTIA, RGMT and MQZG, respectively (Fig. 5). The set  
 218 of ocean tide models considered consists of the three recent global atlases (FES2014b,  
 219 TPX09.v1 and GOT4.10c), FES2012 and EEZ. The latter produces  $\sim 2$  mm residual  
 220 amplitude (purple symbols in Fig. 5) and is, due also to the tide gauge comparison (Ta-  
 221 ble 1), excluded from further analysis. The other models show closer agreement but in  
 222 general the residuals are larger than the estimated 2-sigma uncertainties of the observed  
 223 OTLD when using PREM (Fig. 5, bottom panels). However, we note the similar mag-  
 224 nitude of the variance in  $\|Z_{res}\|$  for all models including EEZ (when the bias is ignored)  
 225 in the up component and complete absence of a  $\|Z_{res}\|$  bias in the horizontal components  
 226 (Fig. S5).

227 Residuals using the purely elastic (original with no corrections) STW105 show a  
 228 similar level of variance and median as PREM (Fig. 4d) while S362ANI shows 50% re-  
 229 duced variance and slightly reduced median (0.48 mm compared with 0.61 mm for PREM).  
 230 However, neither model produces consistent agreement within the GPS uncertainty as

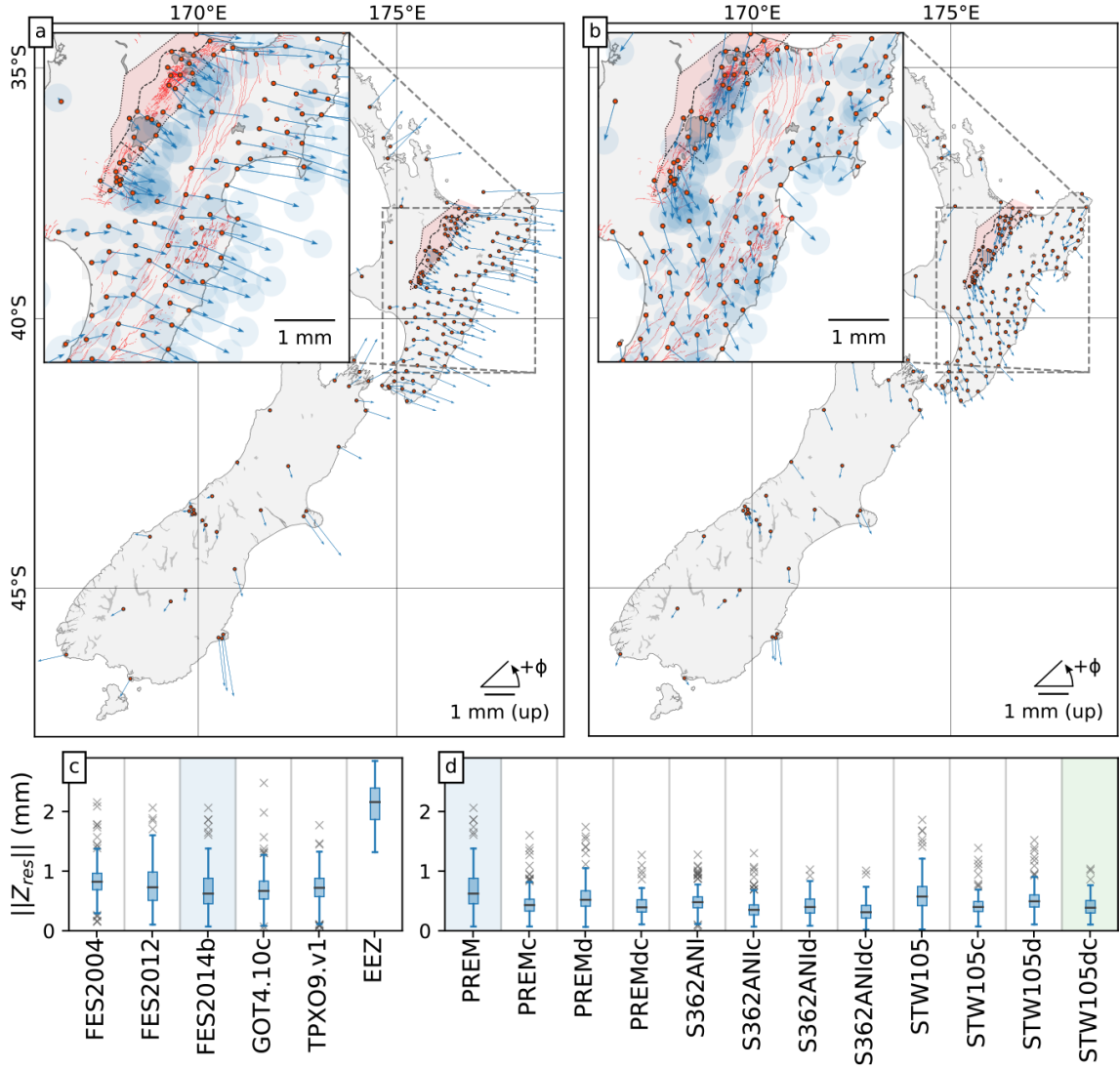


**Figure 4.** M<sub>2</sub> OTLD residuals relative to FES2014b-PREM (a), FES2014-STW105dc (b) with circles on the ends of phasors representing 95% confidence interval of the derived OTLD values. M<sub>2</sub> OTLD residual magnitude ( $\|Z_{res}\|$ ) boxplots for different model setups (c, d). The horizontal line on each box is the median value, the box represents the inter-quartile range (IQR) and the whiskers show an additional  $1.5 \times \text{IQR}$ . Blue and green shading highlights boxplots of (a) and (b) maps, respectively. The Earth model suffixes ‘d’ and ‘c’ in panel (d) refer to the additional treatment of dissipation and compressibility, respectively.

231 shown, for example, with the three sites presented in Fig. 5. We next explore the sensi-  
 232 tivity of the modeled OTLD to anelastic dissipation (denoted suffix “d”), and spatially-  
 233 varying ocean density and compressibility (“c”).

### 234 3.3 Effect of Considering Anelasticity (Dissipation)

235 Bos et al. (2015) demonstrated that accounting for some of the effects of M<sub>2</sub> mantle  
 236 anelasticity by modifying the Green’s functions to include dissipation, decreased OTLD  
 237 residuals in western Europe by up to 0.2 mm. Matviichuk et al. (2020) confirmed these

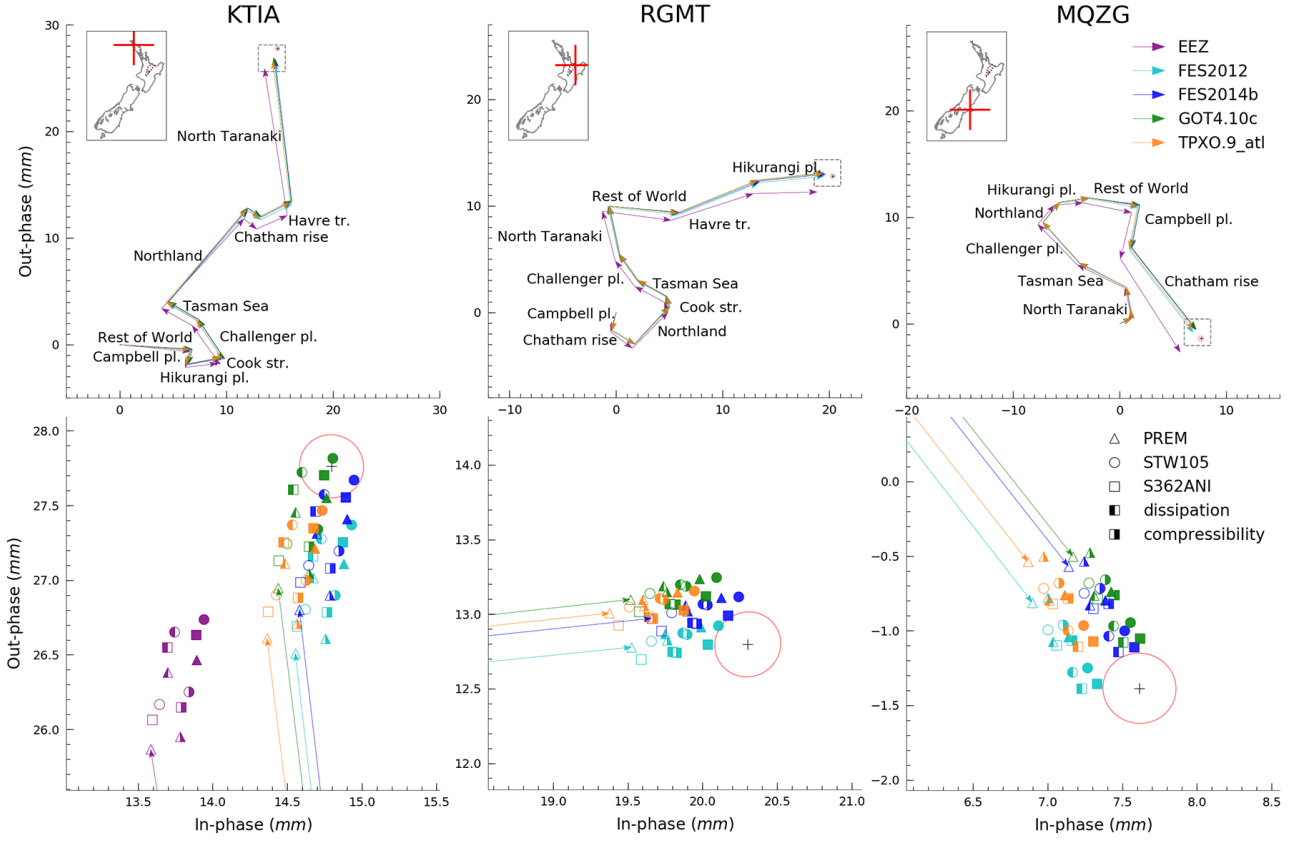


**Figure 5.** Phasor plots of the OTLD contributions from different oceanic regions (see Fig. 2a) for  $M_2$  Up displacements computed with various Green’s functions and ocean tide models. The bottom panels show the detail for the vector tip area shown enclosed by a square in the respective top panels. GPS observations are shown with a black “+” and 95% confidence interval as a red circle. OTLD produced by the are outside the polygons shown in Fig. 2a is titled as “rest of the world”.

**Table 1.** Average  $M_2$  amplitude differences computed over 15 tide gauges relative to a set of ocean tide models.

|                      | FES2004 | FES2012 | FES2014b | GOT4.10c | TPXO.9.atl | EEZ  |
|----------------------|---------|---------|----------|----------|------------|------|
| Avg. difference (cm) | -0.81   | 2.95    | 3.05     | 1.13     | 2.32       | 8.41 |

238 results for the same region but using a different time frame, while similar results have  
 239 been found by Wang et al. (2020) and Martens and Simons (2020) for south-east Asia  
 240 and Alaska, respectively.

241 For New Zealand, we find a reduction of  $\|Z_{res}\|$  variance and median for all Earth  
 242 models when dissipation is included (Fig. 4d). The effect is illustrated in Fig. 5 where  
 243 the models including dissipation (squares with left side only filled) are shown to be closer  
 244 to the GPS estimates. These do, however, remain outside the GPS 95% confidence inter-  
 245 val. At the same time as this improvement, we noticed the introduction of up to 0.2  
 246 mm  $\|Z_{res}\|$  bias into the north component with dissipation enabled, independent of the  
 247 Green’s function used; the east component also shows this effect but only with S362ANI

(Fig. S4). Enabling sea water compressibility correction partially suppresses the bias. We discuss this further below.

### 3.4 Assessment of Water Density and Compressibility Correction

Enabling the seawater compressibility correction decreases the median  $\|Z_{res}\|$  by a further  $\sim 0.2$  mm in the up component, as shown in Fig. 4d and by example in Fig. 5 (fully filled symbols). In some cases, the application of both dissipation and compressibility eliminates the residual in the up component, although as we discuss in the next section, large, regionally coherent residuals persist. Horizontal components show an increase in variance (Fig. S4) with only compressibility considered. The dissipation-introduced  $\|Z_{res}\|$  bias in the north component can be partially (S362ANIdc) or completely (PRE-Mdc, STW105dc) removed by additionally applying the compressibility correction (Fig. S4-5, FES2014b). The east component shows a marginal (less than 0.1 mm) increase in both  $\|Z_{res}\|$  median and variance over the solutions with just dissipation included for PREM and STW105, while S362ANI shows further dissipation-introduced increase in  $\|Z_{res}\|$  bias by another 0.1 mm (Fig. S4).

Following Martens and Simons (2020), we constructed Empirical Cumulative Distribution Function (ECDF) plots (Fig. S7.1) to investigate the impact of corrections on the distribution of  $\|Z_{res}\|$ . The ECDF analysis shows the expected behavior of the corrections in the up component: each correction increases the slope of the ECDF indicating successive improvement with each correction. This is not the case for the horizontal components where both corrections introduce biases using S362ANI, which otherwise demonstrates performance comparable to other models without the corrections. The optimum correction of PREM and STW105 in the north component very much relies on the selection of ocean tide model. The dissipation-introduced bias is suppressed by the compressibility correction in the case of FES2014b and GOT4.10c, which suggests the best performance with both dissipation and compressibility corrections enabled. In the case of TPXO9.v1, the bias is too large for compressibility to overcome, effectively repeating the trend as observed for S362ANI.

Removing the respective mean  $Z_{res}$  values from each set of residuals (Fig. S7.2) aligns the ECDFs over all components, fully removing the differences in the horizontal components with exception for S362ANI-based values in the north component. Removing mean  $Z_{res}$  also absorbs any long-wavelength errors incurred through any mismodeling of the solid Earth body tide.

## 4 Discussion

Following these tests, the optimal agreement between the observed and modeled OTLD in all three components occurs when using FES2014b and STW105dc. The spatial distribution of  $Z_{res}$  shows a spatially coherent signal with amplitude of  $\sim 0.5$  mm over the Taupo Volcanic Zone (TVZ) in the North Island, as shown in Fig. 4. The dense coverage of stations in these regions reveals a distinct change of  $Z_{res}$  between sites in the East Coast (EC) and TVZ that experience the same  $M_2$  OTLD (Fig. 1).

To aid discussion, we consider four different regions (blocks) within this region as illustrated by the symbols in Fig. 6: TVZc, TVZs, ECc, ECs, with “c” and “s” subscripts identifying central and southern subareas, respectively. Residual OTLD in each block was averaged to provide  $Z_{res}$  summary metrics (per component) relevant to each region (Table S6). Note that several sites along the EC were removed (e.g. Hawke Bay) as they experience a localized signal caused mainly by the unmodeled ocean tides (Fig. 6, black symbols) which is independent of the ocean tide model or Green’s function used. The sites in both TVZ regions show residual amplitudes of  $\sim 0.5$  mm with phase changing sharply from  $-102^\circ$  to  $-70^\circ$  between TVZc and TVZs. The relative phase change between TVZ and EC within the same central or south area (TVZc/ECc and TVZs/ECs) is found

298 to be approximately constant ( $\sim 35^\circ$ ) while revealing 0.25 mm and 0.15 mm larger amplitudes for TVZc and TVZs, respectively.  
 299

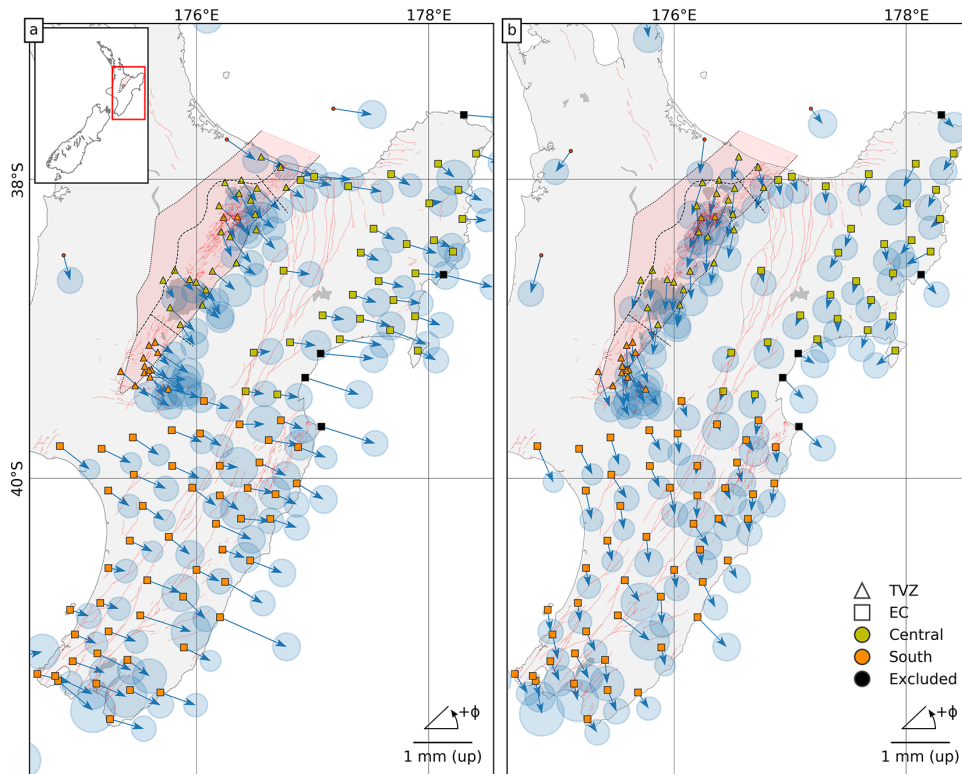


**Figure 6.** GPS-derived  $M_2$  OTLD residuals for a section of the North Island relative to FES2014b ocean tide model combined with dissipation corrected STW105d (a) and STW105dc (b). "d" and "c" suffixes stand for dissipation and compressibility corrections. Sites are categorized into Taupo Volcanic Zone (TVZ) and East Coast (EC) regions (symbol shape) with subdivision of each into central and south along the TVZ central/south boundary (symbol color). Circles on the ends of phasors represent 95% confidence interval of the derived OTLD residuals

300 The sharp change in residual phase between TVZc and TVZs, and the strong spatial  
 301 variation in residual amplitude between respective EC and TVZ sub-regions over length-  
 302 scales of the order of  $\sim 100$  km suggests that the variations are due to localized effects.  
 303 We discount errors in ocean tides given our previous tests and the spatial distribution  
 304 of the residuals. Also, biases in the adopted deep Earth rheological structure (Lau et al.,  
 305 2017) would be effectively constant over this spatial scale.

306 Instead, our assumption is that the residuals result from mismodeled shallow-Earth  
 307 rheological structure. To explore this further, we iterate through a range of alternative  
 308 Earth models, all one-dimensional but with different rheological structure in the upper  
 309 tens of kilometers based on seismic tomography inversions (Eberhart-Phillips & Bannister,  
 310 2015; Eberhart-Phillips & Fry, 2018). No single one-dimensional (radially-varying)  
 311 Earth model could explain the regional pattern of residuals, with changes generally pro-  
 312 ducing changes that were spatially uniform across the region of Fig. 6.

313 Deviations in the shallow rheological structure from that used to compute the Earth  
 314 body tides could produce localized residuals. Zürn et al. (1976) developed a 2D finite-  
 315 element model of a subduction zone in Alaska, and showed that the subduction zone struc-  
 316 ture can produce an effect up to 0.8% on the solid Earth body tide in the radial direc-  
 317 tion directly above the asthenospheric slab. For the  $M_2$  body tide at the latitude of the

318 North Island, this equates to 0.7 mm. However, their modeling also showed that the max-  
 319 imum gradient in the body tide over the distance from East coast to the TVZ (up to 150  
 320 km) should not exceed 0.25% (Zürn et al., 1976, Fig. 5). We note that the effect on phase  
 321 is not described in their work. However, if we consider the relative location of the TVZ  
 322 over the subduction slab (observed by the Vp anomaly at 100-130 km depth (Eberhart-  
 323 Phillips & Fry, 2018)), the maximum expected change becomes close to 0.15%, or 0.13  
 324 mm for  $M_2$  at these latitudes. As such, this is well below the magnitude of the varia-  
 325 tions seen in Fig. 6.

326 The effect of lateral rheological structure on modeled OTLD is unclear. However,  
 327 modeling of elastic deformation due to longer-period surface mass displacement indicates  
 328 that consideration of localized Earth structure produced differences of the order 10% in  
 329 the vertical and 20% in the horizontal over distances of 10-50 km (Dill et al., 2015). The  
 330 average  $M_2$  OTLD in the region of the TVZ shown in Fig. 6 is  $\sim 19$  mm and so even a  
 331 2% effect due to lateral variation may be relevant to explaining the observed residuals.  
 332 Given the minor, but non-negligible effect of lateral variation on Earth body tides, and  
 333 likely effects on OTLD, our analysis suggests that one-dimensional models of this region  
 334 are unlikely to fully explain GPS observations of OTLD at  $M_2$ . To check for potential  
 335 long-wavelength errors that could introduce the observed dissipation-introduced biases  
 336 in the horizontal components, we repeated our analyses for a set of 15 stations in inland  
 337 Australia (see Table S3 for site list and Table S4 for derived observations) where the ge-  
 338 ological setting is simpler and where a 1D model should produce accurate results. For  
 339 this dataset we needed to adopt a different time period (2015-2018 inclusive) due to data  
 340 availability but checking a subset of sites in New Zealand found that the time-period was  
 341 inconsequential. Figures S9 and S10 demonstrate that, although the magnitude of the  
 342 OTLD is still several mm, for these stations the residuals (observed minus predicted OTLD)  
 343 are indeed small and within the uncertainty of the observations. This validates the ro-  
 344 bustness of our analyses and suggests that tidal centre-of-mass errors in this region are  
 345 small, specifically for FES2014b and GOT4.10c ocean tide models.

346 Figures S7.1 and S7.2 show that the OTLD residuals for the horizontal components  
 347 suffer from a common mode issue that modification of the Green's function cannot over-  
 348 come. For the up component, the influence of the dissipation effect within asthenosphere  
 349 that requires us to modify the elastic properties of the Earth model from the reference  
 350 period of 1s to tidal periods is noticeable. Furthermore, including spatially varying sea-  
 351 water density and compressibility results in an additional reduction of the misfit. These  
 352 two figures also demonstrate that the difference between the ocean tide models used in  
 353 the loading computations is small. Therefore, the most likely candidate to reduce the  
 354 misfit further is to use an advanced (3D) (an)elastic model of the region.

355 Similar problems using a 1D Earth modeling OTLD in Alaska were recently de-  
 356 scribed by Martens and Simons (2020). We are unaware of three-dimensional models be-  
 357 ing in use for the computation of OTLD, however Latychev et al. (2009) have computed  
 358 Earth body tides with a three-dimensional model. One practical consequence of this is  
 359 that mismodeled tidal deformations in this region will propagate into conventional 24  
 360 hr coordinate solutions (Penna et al., 2007). Such propagation will introduce long-period  
 361 noise in GPS coordinate time series in New Zealand and impact subsequent geophysi-  
 362 cal interpretation.

## 363 5 Conclusions

364 We estimate  $M_2$  ocean tide loading displacements (OTLD) at 170 GPS sites in New  
 365 Zealand from the beginning of 2013 to mid-2020 (doy 153). Comparison with modeled  
 366 OTLD displacements using a range of global tide models and elastic PREM shows sub-  
 367 mm agreement, with much larger disagreements when using a local New Zealand tide  
 368 model.

369 However, on close inspection we find that no single one-dimensional elastic Earth  
 370 model, when combined with modern global tide models, can consistently explain the GPS-

371 derived OTLD within uncertainties. Of the tested ocean tide models, FES2014b produced  
 372 the best results. However, application of an anelastic dissipation correction, and vary-  
 373 ing water density and compressibility substantially improves the agreement between the  
 374 various models and observed OTLD. Despite this, some regional spatially-coherent un-  
 375 modeled residual signals remain in the North Island with magnitudes of up to 0.3 mm.  
 376 These show substantial variation in phase over  $\sim 100$  km in the region between the Taupo  
 377 Volcanic Zone and the East coast. We attempted to reproduce the observed signal us-  
 378 ing a range of 1D Earth models with varying shallow Earth structures, including the ef-  
 379 fects of anelasticity, however no single model could explain the residuals. We anticipate  
 380 that these residuals are a result of unmodeled lateral variations in Earth rheological struc-  
 381 ture forced largely by ocean tide loading but with a smaller component likely from mis-  
 382 modeled Earth body tides.

383 This analysis of residual OTLD demonstrates the deficiencies of the 1D Earth mod-  
 384 eling approach that is currently standard practice. This is particularly relevant to GPS  
 385 analysis using 24 hr coordinate solutions, given mismodeled tidal displacements prop-  
 386 agate into long-period signal. Utilizing 3D Earth modeling to compute tidal phenom-  
 387 ena is likely required to explain the observations in regions with major discontinuities  
 388 in Earth’s lateral structure (e.g. subduction margins). Such models, combined with these  
 389 observations, could provide new insights into the shallow rheological structure of these  
 390 regions.

### 391 Acknowledgments

392 We greatly acknowledge the New Zealand GeoNet project and its sponsors EQC, GNS  
 393 Science and LINZ, and Geoscience Australia for providing the data used in this study.  
 394 We are grateful to NASA Jet Propulsion Laboratory for GipsyX software, products and  
 395 support. The services of TPAC High Performance Computing Facility are acknowledged  
 396 gratefully. We thank Klaus Schueller for advice and discussion on Eterna software. We  
 397 acknowledge the support of Elisabetta D’Anastasio in accessing the data and site logs.

398 Bogdan Matviichuk is supported by Tasmania Graduate Research Scholarship. MSB  
 399 is supported by the project FCT/UIDB/50019/2020 – IDL funded by FCT.

400 GipsyX binaries were provided under license from JPL. Eterna tidal analysis and  
 401 prediction software with source code was acquired from International Geodynamics and  
 402 Earth Tide Service (IGETS), [igets.u-strasbg.fr/soft\\_and\\_tool.php](http://igets.u-strasbg.fr/soft_and_tool.php). The RINEX  
 403 files can be acquired from [ftp.geonet.org.nz](http://ftp.geonet.org.nz), coordinate time series are provided at  
 404 [data.utas.edu.au/metadata/ff80025e-0019-4cbb-aa8a-2fb289915b51](http://data.utas.edu.au/metadata/ff80025e-0019-4cbb-aa8a-2fb289915b51). Figures 1 and  
 405 2 use perceptually uniform color maps of Crameri et al. (2020).

### 406 References

- 407 Abbaszadeh, M., Clarke, P. J., & Penna, N. T. (2020). Benefits of combining GPS  
 408 and GLONASS for measuring ocean tide loading displacement. *Journal of*  
 409 *Geodesy*, *94*(7), 63. doi: 10.1007/s00190-020-01393-5
- 410 Alterman, Z., Jarosch, H., Pekeris, C. L., & Jeffreys, H. (1959). Oscillations of the  
 411 earth. *Proceedings of the Royal Society of London. Series A. Mathematical and*  
 412 *Physical Sciences*, *252*(1268), 80–95. doi: 10.1098/rspa.1959.0138
- 413 Bertiger, W., Bar-Sever, Y., Dorsey, A., Haines, B., Harvey, N., Hemberger, D.,  
 414 ... Willis, P. (2020). GipsyX/RTGx, a new tool set for space geodetic op-  
 415 erations and research. *Advances in Space Research*, *66*(3), 469–489. doi:  
 416 10.1016/j.asr.2020.04.015
- 417 Bertiger, W., Desai, S. D., Haines, B., Harvey, N., Moore, A. W., Owen, S., & Weiss,  
 418 J. P. (2010). Single receiver phase ambiguity resolution with GPS data.  
 419 *Journal of Geodesy*, *84*(5), 327–337. doi: 10.1007/s00190-010-0371-9
- 420 Bos, M. S., & Baker, T. F. (2005). An estimate of the errors in gravity ocean tide  
 421 loading computations. *Journal of Geodesy*, *79*(1), 50–63. doi: 10.1007/s00190

- 422 -005-0442-5
- 423 Bos, M. S., Penna, N. T., Baker, T. F., & Clarke, P. J. (2015). Ocean tide loading  
424 displacements in western europe: 2. gps-observed anelastic dispersion in the as-  
425 thenosphere. *Journal of Geophysical Research: Solid Earth*, *120*(9), 6540–6557.  
426 doi: 10.1002/2015JB011884
- 427 Bos, M. S., & Scherneck, H.-G. (2013). Computation of Green’s Functions for Ocean  
428 Tide Loading. In G. Xu (Ed.), *Sciences of Geodesy - II* (pp. 1–52). Berlin,  
429 Heidelberg: Springer Berlin Heidelberg. doi: 10.1007/978-3-642-28000-9\_1
- 430 Carrere, L., Lyard, F., Cancet, M., Guillot, A., & Dupuy, S. (2016). Fes 2014 : a  
431 new global tidal model. , 8.
- 432 Carrere, L., Lyard, F., Cancet, M., Guillot, A., & Roblou, L. (2013). Fes 2012: A  
433 new global tidal model taking advantage of nearly 20 years of altimetry. In *20*  
434 *years of progress in radar altimetry* (Vol. 710, p. 13).
- 435 Cramer, F., Shephard, G. E., & Heron, P. J. (2020). The misuse of colour in science  
436 communication. *Nature Communications*, *11*, 5444. doi: 10.1038/s41467-020-  
437 -19160-7
- 438 Desai, S. D., & Ray, R. D. (2014). Consideration of tidal variations in the geocenter  
439 on satellite altimeter observations of ocean tides. *Geophysical Research Letters*,  
440 *41*(7), 2454–2459. doi: 10.1002/2014GL059614
- 441 Dill, R., Klemann, V., Martinec, Z., & Tesauro, M. (2015). Applying local  
442 green’s functions to study the influence of the crustal structure on hydro-  
443 logical loading displacements. *Journal of Geodynamics*, *88*, 14–22. doi:  
444 10.1016/j.jog.2015.04.005
- 445 Dziewonski, A. M., & Anderson, D. L. (1981). Preliminary reference earth  
446 model. *Physics of the Earth and Planetary Interiors*, *25*(4), 297–356. doi:  
447 10.1016/0031-9201(81)90046-7
- 448 Eberhart-Phillips, D., & Bannister, S. (2015). 3-D imaging of the northern Hiku-  
449 rangi subduction zone, New Zealand: variations in subducted sediment, slab  
450 fluids and slow slip. *Geophysical Journal International*, *201*(2), 838–855. doi:  
451 10.1093/gji/ggv057
- 452 Eberhart-Phillips, D., & Fry, B. (2018). Joint local earthquake and teleseismic in-  
453 version for 3-D velocity and Q in New Zealand. *Physics of the Earth and Plan-  
454 etary Interiors*, *283*, 48–66. doi: 10.1016/j.pepi.2018.08.005
- 455 Egbert, G. D., & Erofeeva, S. Y. (2002). Efficient Inverse Modeling of Barotropic  
456 Ocean Tides. *Journal of Atmospheric and Oceanic Technology*, *19*(2), 183–204.  
457 doi: 10.1175/1520-0426(2002)019<0183:EIMOBO>2.0.CO;2
- 458 Farrell, W. E. (1972a). Deformation of the earth by surface loads. *Reviews of Geo-  
459 physics*, *10*(3), 761–797. doi: 10.1029/RG010i003p00761
- 460 Farrell, W. E. (1972b). Global Calculations of Tidal Loading. *Nature Physical Sci-  
461 ence*, *238*(81), 43–44. doi: 10.1038/physci238043a0
- 462 Gale, N., Gledhill, K., Chadwick, M., & Wallace, L. (2015). The Hikurangi Mar-  
463 gin Continuous GNSS and Seismograph Network of New Zealand. *Seismologi-  
464 cal Research Letters*, *86*(1), 101–108. doi: 10.1785/0220130181
- 465 Guo, J.-Y., Ning, J.-S., & Zhang, F.-P. (2001). Chebyshev-collocation method ap-  
466 plied to solve odes in geophysics singular at the earth center. *Geophysical Re-  
467 search Letters*, *28*(15), 3027–3030. doi: 10.1029/2001GL012886
- 468 Hu, Y., Bürgmann, R., Banerjee, P., Feng, L., Hill, E. M., Ito, T., . . . Wang, K.  
469 (2016). Asthenosphere rheology inferred from observations of the 2012 indian  
470 ocean earthquake. *Nature*, *538*(7625), 368–372. doi: 10.1038/nature19787
- 471 Ito, T., & Simons, M. (2011). Probing asthenospheric density, temperature, and  
472 elastic moduli below the western united states. *Science*, *332*(6032), 947–951.  
473 doi: 10.1126/science.1202584
- 474 Karato, S.-i. (2012). On the origin of the asthenosphere. *Earth and Planetary Sci-  
475 ence Letters*, *321-322*, 95–103. doi: 10.1016/j.epsl.2012.01.001
- 476 Kustowski, B., Ekström, G., & Dziewoński, A. M. (2008). Anisotropic shear-wave

- 477 velocity structure of the earth’s mantle: A global model. *Journal of Geophysical*  
 478 *Research: Solid Earth*, 113(B6). doi: 10.1029/2007JB005169
- 479 Lamarche, G., & Lebrun, J.-F. (2000). Transition from strike-slip faulting to oblique  
 480 subduction: active tectonics at the puysegur margin, south new zealand.  
 481 *Tectonophysics*, 316(1), 67–89. doi: 10.1016/S0040-1951(99)00232-2
- 482 Latychev, K., Mitrovica, J. X., Ishii, M., Chan, N.-H., & Davis, J. L. (2009). Body  
 483 tides on a 3-D elastic earth: Toward a tidal tomography. *Earth and Planetary*  
 484 *Science Letters*, 277(1), 86–90. doi: 10.1016/j.epsl.2008.10.008
- 485 Lau, H. C. P., Mitrovica, J. X., Davis, J. L., Tromp, J., Yang, H.-Y., & Al-Attar, D.  
 486 (2017). Tidal tomography constrains Earth’s deep-mantle buoyancy. *Nature*,  
 487 551(7680), 321–326. doi: 10.1038/nature24452
- 488 Lyard, F., Lefevre, F., Letellier, T., & Francis, O. (2006). Modelling the global  
 489 ocean tides: modern insights from FES2004. *Ocean Dynamics*, 56(5-6), 394–  
 490 415. doi: 10.1007/s10236-006-0086-x
- 491 Martens, H. R., & Simons, M. (2020). A comparison of predicted and observed  
 492 ocean tidal loading in alaska. *Geophysical Journal International*, ggaa323. doi:  
 493 10.1093/gji/ggaa323
- 494 Martens, H. R., Simons, M., Owen, S., & Rivera, L. (2016). Observations of ocean  
 495 tidal load response in south america from subdaily gps positions. *Geophysical*  
 496 *Journal International*, 205(3), 1637–1664. doi: 10.1093/gji/ggw087
- 497 Matviichuk, B. (2020). *GipsyX Wrapper: v0.1.0*. doi: 10.5281/zenodo.4001166
- 498 Matviichuk, B., King, M., & Watson, C. (2020). Estimating ocean tide loading dis-  
 499 placements with GPS and GLONASS. *Solid Earth*, 11(5), 1849–1863. doi: 10  
 500 .5194/se-11-1849-2020
- 501 Penna, N. T., Clarke, P. J., Bos, M. S., & Baker, T. F. (2015). Ocean tide load-  
 502 ing displacements in western europe: 1. validation of kinematic gps esti-  
 503 mates. *Journal of Geophysical Research: Solid Earth*, 120(9), 6523–6539.  
 504 doi: 10.1002/2015JB011882
- 505 Penna, N. T., King, M. A., & Stewart, M. P. (2007). Gps height time series: Short-  
 506 period origins of spurious long-period signals. *Journal of Geophysical Research:*  
 507 *Solid Earth*, 112(B2). doi: 10.1029/2005JB004047
- 508 Petit, G., & Luzum, B. (2010). IERS Conventions (2010). (36), 179.
- 509 Ray, R. D. (2013). Precise comparisons of bottom-pressure and altimetric ocean  
 510 tides: Bottom-pressure and altimetric tides. *Journal of Geophysical Research:*  
 511 *Oceans*, 118(9), 4570–4584. doi: 10.1002/jgrc.20336
- 512 Stammer, D., Ray, R. D., Andersen, O. B., Arbic, B. K., Bosch, W., Carrère, L., . . .  
 513 Yi, Y. (2014). Accuracy assessment of global barotropic ocean tide models.  
 514 *Reviews of Geophysics*, 52(3), 243–282. doi: 10.1002/2014RG000450
- 515 Stern, R. (2004). Subduction initiation: spontaneous and induced. *Earth and Plane-*  
 516 *tary Science Letters*, 226(3-4), 275–292. doi: 10.1016/S0012-821X(04)00498-4
- 517 Walters, R. A., Goring, D. G., & Bell, R. G. (2001). Ocean tides around New  
 518 Zealand. *New Zealand Journal of Marine and Freshwater Research*, 35(3),  
 519 567–579. doi: 10.1080/00288330.2001.9517023
- 520 Wang, J., Penna, N. T., Clarke, P. J., & Bos, M. S. (2020). Asthenospheric anelas-  
 521 ticity effects on ocean tide loading around the east china sea observed with  
 522 gps. *Solid Earth*, 11(1), 185–197. doi: 10.5194/se-11-185-2020
- 523 Wenzel, H.-G. (1996). The nanogal software : Earth tide data processing package  
 524 ETERNA 3.30. *Bull. Inf. Marées Terrestres*, 124, 9425–9439.
- 525 Wessel, P., & Smith, W. H. F. (1996). A global, self-consistent, hierarchical, high-  
 526 resolution shoreline database. *Journal of Geophysical Research: Solid Earth*,  
 527 101(B4), 8741–8743. doi: 10.1029/96JB00104
- 528 Yuan, L., & Chao, B. F. (2012). Analysis of tidal signals in surface displacement  
 529 measured by a dense continuous gps array. *Earth and Planetary Science Let-*  
 530 *ters*, 355-356, 255–261. doi: 10.1016/j.epsl.2012.08.035
- 531 Yuan, L., Chao, B. F., Ding, X., & Zhong, P. (2013). The tidal displacement field at

- 532 earth's surface determined using global gps observations: Tidal displacements  
533 determined by gps. *Journal of Geophysical Research: Solid Earth*, 118(5),  
534 2618–2632. doi: 10.1002/jgrb.50159
- 535 Zumberge, J. F., Heflin, M. B., Jefferson, D. C., Watkins, M. M., & Webb, F. H.  
536 (1997). Precise point positioning for the efficient and robust analysis of gps  
537 data from large networks. *Journal of Geophysical Research: Solid Earth*,  
538 102(B3), 5005–5017. doi: 10.1029/96JB03860
- 539 Zweng, M. M., Reagan, J. R., Antonov, J. I., Locarnini, R. A., Mishonov, A. V.,  
540 Boyer, T. P., . . . Levitus, S. (2013). World ocean atlas 2013. Volume 2, Salin-  
541 ity.. doi: 10.7289/V5251G4D
- 542 Zürn, W., Beaumont, C., & Slichter, L. B. (1976). Gravity tides and ocean load-  
543 ing in southern alaska. *Journal of Geophysical Research (1896-1977)*, 81(26),  
544 4923–4932. doi: 10.1029/JB081i026p04923